International Journal of
Turbomachinery
Propulsion and Power

MDPI

Article

Experimental Results in a Variable-Pitch Wells Rotor †

Fabio Licheri *, Tiziano Ghisu, Francesco Cambuli, Pierpaolo Puddu and Mario Carta

Department of Mechanical, Chemical and Materials Engineering (DIMCM), University of Cagliari, Via Marengo 2, 09123 Cagliari, Italy

* Correspondence: fabio.licheri@unica.it; Tel.: +39-070-6755724

† This paper is an extended version of our paper published in the Proceedings of the 16th European Turbomachinery Conference, Hannover, Germany, 24–28 March 2025.

Abstract: Systems based on the oscillating water column (OWC) principle are often equipped with Wells turbines as power take-offs (PTOs) to convert sea-wave energy. The self-rectifying nature of the Wells turbine represents a strength for such applications, while its limited operating range, due to stall, is one of the most relevant limitations. A possible improvement lies in varying the blade stagger angle during operation as this can delay stall by reducing the incidence angle. Although the performance of variable-pitch Wells turbines has been studied in the past, their local aerodynamic performance has never been investigated before. This study addresses this important task by experimentally reconstructing the flow field along the blade height of a Wells turbine prototype, coupled to an OWC simulator, for three values of the stagger angle. The aerodynamic behavior of the Wells rotor is characterized at its inlet and outlet, showing how the interaction between adjacent blades changes due to the stagger angle. The rotor performance is evaluated and compared, providing useful information that is of general validity for similar rows of symmetric blade profiles when pitched at different stagger angles.

Keywords: Wells turbines; variable-pitch rotor; performance improvement; experimental measurements; 3D local flow; efficiency

Received: 9 April 2025
Revised: 22 April 2025
Accepted: 5 June 2025
Published: 11 June 2025

Citation: Licheri, F.; Ghisu, T.; Cambuli, F.; Puddu, P.; Carta, M. Experimental Results in a Variable-Pitch Wells Rotor. *Int. J. Turbomach. Propuls. Power* **2025**, *10*, 10. https://doi.org/10.3390/ijtpp10020010

1. Introduction

Large availability [1] and relatively slow time variance, if compared to more common renewable energy sources [2], are the most relevant strengths that have attracted researchers to wave energy. Despite the large number of wave energy converters (WECs) proposed and designed during the last few decades [3,4], wave energy technology is not commercially mature, mainly due to the high costs [5] associated with installation, operation, and maintenance in such a critical environment as the marine offshore [2]. Among all studied and developed solutions, those based on the oscillating water column (OWC) principle are generally recognized as highly reliable and simple to construct and operate [6] thanks to the absence of moving parts submerged in the sea [7]. Moreover, the possibility to install WECs based on the OWC principle in breakwater structures significantly reduces the installation and maintenance costs [8].

The operation of WECs based on the OWC principle, as schematized in Figure 1, consists of two subsequent stages of energy conversion. The wave motion confined to an open chamber that is partially submerged in water establishes an airflow through a duct placed at the top of the chamber, characterized by non-stationary and alternate behavior. Then, a power take-off (PTO)—generally an air turbine—converts the pneumatic energy stored in the airflow into mechanical energy at its shaft, which is finally converted into electric energy by means of a generator.

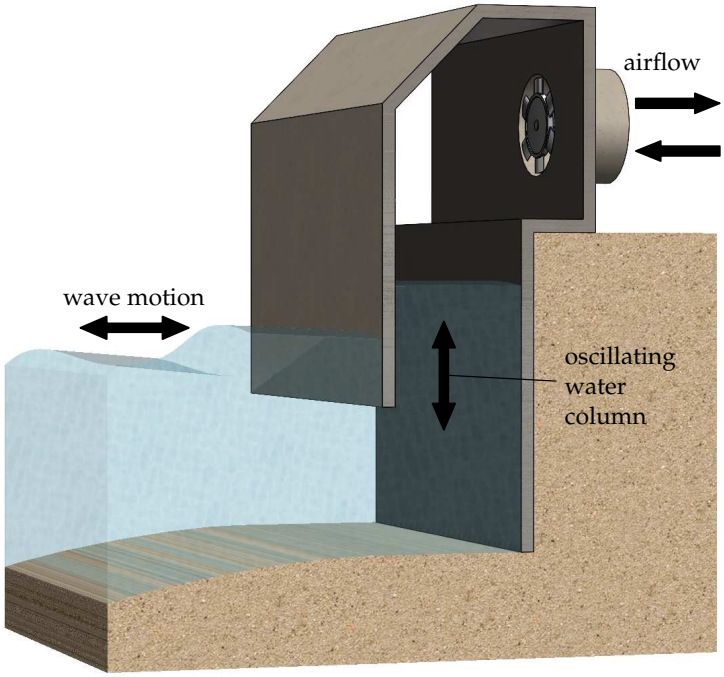

Figure 1. Working principle of an OWC device.

The Wells rotor [9] is one of the most interesting turbines that has been coupled with OWC-based WECs [10,11] thanks to its self-rectifying behavior, obtained with a symmetrical blade profile, typically from the NACA four-digit series, staggered at 90 degrees with respect to its axis of rotation. This uncommon blade design allows the machine to rotate in the same direction regardless of the flow direction. This results in a simple construction, not requiring additional components such as valves or stator blades, which are necessary when adopting conventional turbines [12]. During the last 50 years, Wells turbines have been installed in WECs [13,14] and investigated in detail to characterize their performance [15,16] and to find solutions to overcome the most relevant limitations—in particular, the narrow range of operation due to stall [17].

As the stall phenomenon is associated with flow separation at high incidence angles [18], two possible solutions to delay stall for large flow rates are typically used in turbomachinery: variable-speed- and variable-pitch-controlled rotors. Speed-controlled Wells turbines have been widely investigated, using both simulation approaches [19,20] and experiments [21,22], showing the possibility to not only extend the stable operating range of the machine but also to improve the average power production and the rotor performance. Other control strategies have been proposed to directly regulate the flow rate [23] by acting on properly designed regulating valves placed at the air turbine–OWC interface.

A monoplane Wells turbine with variable-pitch blades [24], whose working principle is schematized in Figure 2, represents a challenging solution due to the difficulty in controlling the blade stagger angle of a rotating machine during operation under a bidirectional airflow. Nevertheless, studies have been conducted with the aim of the initial characterization of the rotor performance for different values of the blade stagger angle, under both stationary [25–29] and non-stationary flow conditions [30,31]. Based on this information, control strategies have been proposed and simulated both under regular [30] and irregular wave conditions [32]. A full-scale variable-pitch Wells turbine was designed in the late 1990s [33] for the Pico Wave Power Plant, but it was never installed [34].

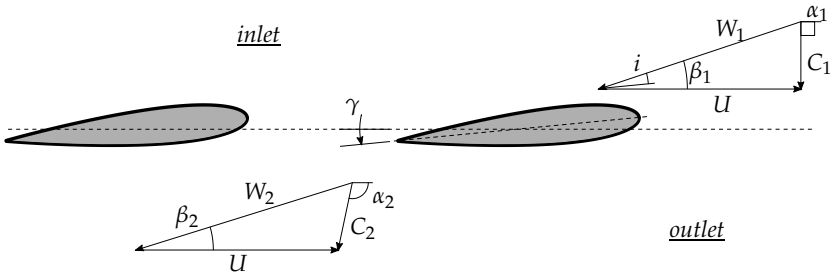

Figure 2. Velocity triangles for a variable-pitch Wells row.

All existing experimental research, to the best of the authors' knowledge, has been conducted on rotors with fixed blades staggered at different angles and tested under stationary flow conditions. The aim of these investigations was to aerodynamically characterize the turbines, providing useful indications for the definition of a control strategy to avoid stall occurrence. Nevertheless, no information is available regarding the local flow behavior and the non-stationary operation of non-zero staggered Wells turbines. This paper presents, for the first time, the detailed characterization of the local aerodynamic behavior of a variable-pitch Wells turbine coupled to an OWC simulator, for three different values of the blade stagger angle, kept fixed during the experiments. The rotor prototype, designed and built at the Department of Mechanical, Chemical, and Materials Engineering (DIMCM) of the University of Cagliari, has been tested under regular wave conditions with an existing experimental apparatus [35–37]. A mechanism was used to orient the rotating blades synchronously by acting on a stepper motor. Global and local performance has been determined using a four-hole pressure probe, referred to in the remainder of this paper as the 'DIMCM probe', to characterize the inlet and outlet mean flow fields along the blade height.

The results presented in this work, which is an extension of our meeting paper [38], offer important insights into the behavior of a variable-pitch Wells turbine, explaining how the Wells row works with stagger angles other than 90 degrees with respect to the axis of rotation. The information provided through these detailed measurements is useful to define a control strategy for performance maximization based on variations in the blade stagger angle, showing the capabilities and limitations of such a control approach in improving the Wells turbine's performance. Moreover, the local analyses presented in this work are of general validity, enabling us to understand how this type of blade row works, given the intrinsic complexity in reproducing similar experiments using traditional wind tunnel linear cascades.

2. Experimental Setup and Procedure

The turbomachinery laboratory at the University of Cagliari houses an OWC simulator that can be coupled to Wells turbines, allowing one to characterize the rotor performance under a non-stationary bidirectional flow representative of the one inside a real OWC. The complete setup is schematized in Figure 3.

It consists of a vertical cylindrical steel chamber where a piston moves, driven by a hydraulic power unit. Regular wave motion is typically reproduced, as shown in Figure 4, by setting both the piston stroke amplitude and the wave period T_w according to the required maximum flow rate for the turbine under test.

The Wells turbine prototype is placed at the top of the chamber and connected to an electric motor/generator driven by an inverter that controls its rotational speed during operation. The variable-pitch turbine is equipped with a mechanism controlled by a stepper motor that allows one to simultaneously rotate all of the blades around their pivoting axis, varying their stagger angles within a range of ± 15 degrees with respect to the traditional

non-staggered position, with a maximum positioning error of ±0.5 degrees. The turbine's most important geometric parameters are summarized in Table 1.

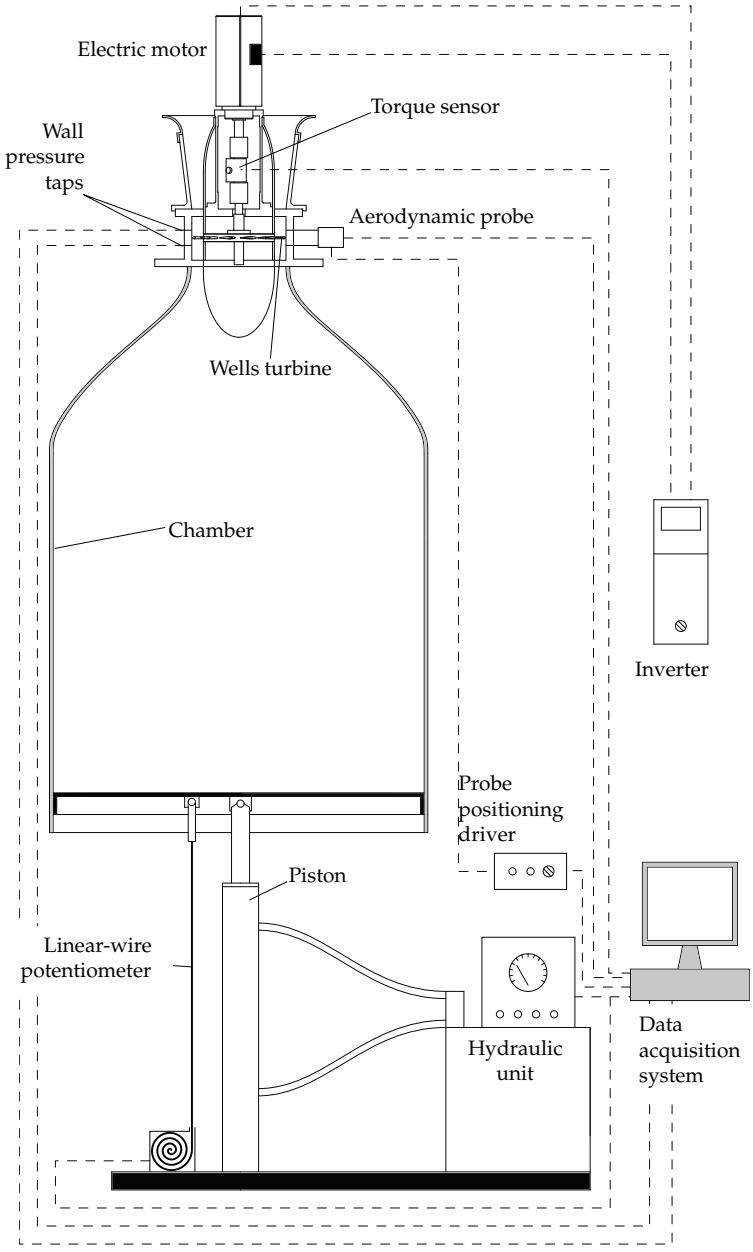

Figure 3. Schematic view of the experimental setup.

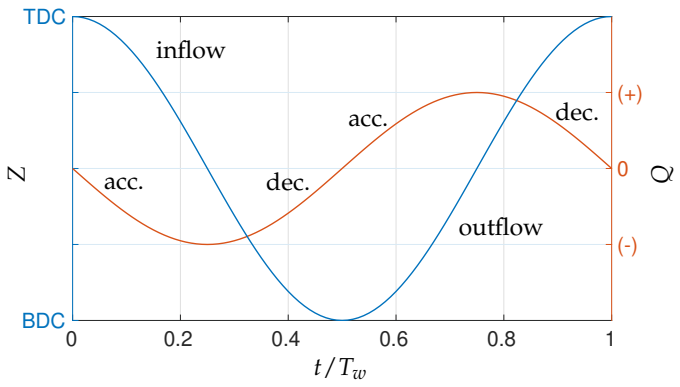

Figure 4. Piston displacement and flow rate for regular wave motion.

Table 1. Geometry of the variable-pitch Wells turbine.

rotor tip radius, r_{tip}	124.7 mm
rotor hub radius, r_{hub}	95 mm
chord length, c	36 mm
number of blades, z	14
airfoil profile	NACA 0015
rotor solidity	0.729
tip-gap-to-chord ratio, t/c	4.4%
hub-to-tip ratio, ν	0.76
sweep ratio	15/36

Wells turbines' performance is generally described using the following non-dimensional parameters:

$$p^* = \frac{\Delta p}{\rho \Omega^2 r_{tip}^2}$$
$$T^* = \frac{T}{\rho \Omega^2 r_{tip}^5}$$
$$\phi = \frac{V_{flow}}{\Omega r_{tip}} \quad (1)$$
$$\eta = \frac{T\Omega}{\Delta p Q} = \frac{T^*}{p^* \phi} \frac{1}{\pi(1-\nu^2)}$$

These denote the pressure coefficient p^*, the torque coefficient T^*, the flow coefficient ϕ, and the efficiency η, respectively. With the aim of evaluating these parameters, the rotor torque T is measured using a torque sensor placed between the turbine's shaft and the electric machine, the rotational speed is detected using an optical encoder, and the pressure drop across the rotor Δp is taken using two sets of wall pressure taps placed at an axial distance of 7.5 mm from the blade pivoting axis, both upstream and downstream of the rotor. The flow rate Q is not measured using standardized flow meters, due to the setup arrangement, but it is calculated based on the acquisition of the piston position using a wire potentiometer. Hence, Q is evaluated knowing the geometry of the chamber and taking into account the capacitive delay between the piston speed and the airflow speed V_{flow}, due to the presence of the chamber volume [35,39].

The turbine's local performance can be determined from the aerodynamic behavior of the rotor, i.e., by reconstructing the mean flow velocity components at the inlet and the outlet of the rotor along the blade height. The experimental apparatus allows aerodynamic probes to be placed near the rotor, at different axial stations. In this work, the mean local flow has been characterized using a 4-hole pressure probe, already employed in a previous work [36] where a conventional Wells turbine was tested. The DIMCM probe, sketched in Figure 5, has a relatively small head size, with a maximum size of 2.5 mm in the radial direction and a stem diameter of 3 mm, and it allows one to reconstruct the mean three-dimensional velocity components along the blade span. It has been placed at both the inlet and outlet of the rotor, at an axial distance of $\pm$15 mm from the blade pivot axis. (As with other conventional aerodynamic probes, it is not able to reconstruct the instantaneous flow field along the rotor blade pitch.)

The probe has been used to evaluate the flow angles, in the radial and tangential planes, and both the total and static pressures, using the 'non-nulling' positioning mode. The calibration procedure has been conducted in a subsonic wind tunnel in order to characterize the response of the DIMCM probe, introducing the non-dimensional parameters typically used for other multi-hole aerodynamic probes [40]. A detailed description of the calibration coefficients for the actual probe can be found in [36]. The maximum uncertainties have been

estimated for both the flow angles, around ±0.5 degrees, and the flow speed calculated using the reconstructed static and total pressures, ±0.5 m/s. The probe's settling time has been verified to be smaller than the value prescribed by the Nyquist rate [41] of the non-stationary flow reproduced with the OWC simulator (characterized by a time period of 7 s, as listed in Table 2), ensuring the correct reconstruction of temporal flow variations. Additional information about the DIMCM probe can be found in a recent work from the authors [36].

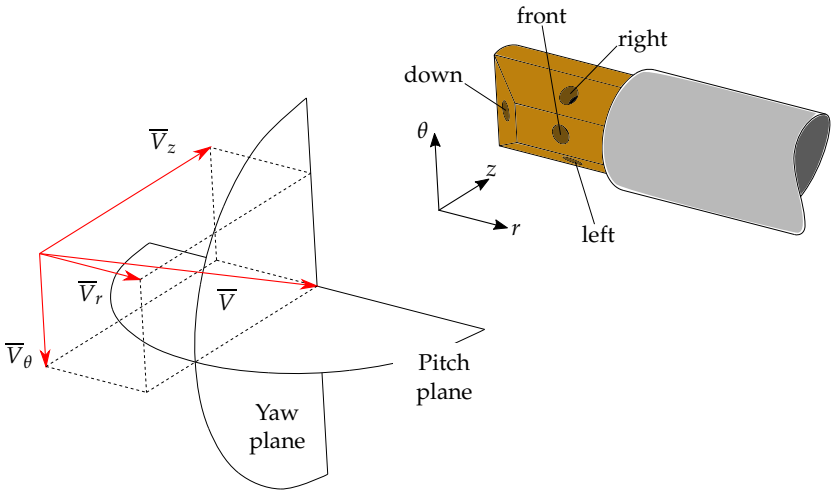

Figure 5. DIMCM probe: schematic view and measured components.

Starting from the flow characterization in terms of flow angles and velocity components, the local performance can be evaluated by introducing the work coefficient ψ, the relative total pressure loss coefficient Y_P, and the loss coefficient due to exit kinetic energy ξ_{EX}, as proposed in [42,43] and adapted to Wells turbine analysis in [44].

$$\begin{aligned} \psi &= \frac{U\,(C_{\theta,1} - C_{\theta,2})}{U_{tip}^2} \\ Y_P &= \frac{(P_1 - P_2)_{rel}}{{}^1\!/_2\,\rho_2\,W_2^2} \\ \xi_{EX} &= \frac{C_2^2/2}{h_{t,1} - h_{is,2}} \end{aligned} \tag{2}$$

where $P_1 - P_2$ is the relative total pressure drop, and $h_{t,1} - h_{is,2}$ represents the total energy available through an isentropic expansion. The complete derivation of the coefficients in Equation (2) can be found in [44].

Three different rotor geometries, obtained by fixing the blade stagger angle at different values, have been tested under the same non-stationary operating conditions. Sinusoidal piston motion, whose main characteristics are summarized in Table 2, has been reproduced in the OWC simulator, while the rotational speed of the rotors has been kept constant.

Table 2. Operating settings used for the experiments.

blade stagger angle, γ	0–5–10 deg
piston period, T_w	7 s
stroke amplitude	≈850 mm
turbine rotational frequency, f	45 Hz
number of radial probe positions	13
number of acquired periods per position	7
sampling rate	200 Hz

The maximum Reynolds number of the relative flow at the rotor outlet, calculated based on the blade chord, is equal to $\approx 1.25 \times 10^5$. Limited variations have been observed during turbine operation due to the fact that the relative velocity is always close to the constant rotor peripheral speed.

The blade stagger angle has been set in order to reduce the flow incidence during the inflow phase, and the local measurements have been performed only with the flow coming from the ambient side into the OWC chamber. A total of 13 radial stations have been used to scan the flow in the blade height, performing smaller steps near the walls than in the center of the channel, where low gradients were expected for all acquired quantities.

All signals, both from the probe and from the other transducers, have been acquired with a sampling frequency of 200 Hz for at least 7 piston periods, in order to perform a phase-locked averaging process based on the sinusoidal piston position. The signals have then been resampled, extracting 250 equally spaced points in the averaged piston period. As the global measurements were acquired at each probe's radial position, they have been averaged over a total of 7×13 piston periods. This process has been proven to reduce the noise found in torque and rotational speed measurements that are affected by larger fluctuations due to the nature of the corresponding signals.

The measurement uncertainties for the averaged signals have been evaluated and propagated using the uncertainty propagation method (UPM) [45] in order to discern the maximum errors expected for the performance coefficients in Equation (1). As a result, a maximum uncertainty of $\pm 2.9\%$ has been observed for the torque coefficient T^*, a value of $\pm 0.8\%$ for the pressure coefficient p^*, and a value of $\pm 1.5\%$ for the flow coefficient ϕ. As the efficiency η is a combination of all of the above non-dimensional performance aspects (see Equation (1)), its maximum uncertainty is slightly larger and is equal to $\pm 3.2\%$.

3. Results

3.1. Global Performance for a Complete Piston Period

The global performance of the Wells rotor during a complete piston period is reported in Figure 6 for three values of the blade stagger angle γ. Coefficient curves have been fitted using a Gaussian-weighted average to smooth noise in the efficiency calculations.

These representations highlight the differences between the inflow and outflow phases, which become larger when the value of the stagger angle (fixed during every test) is increased, as it produces a reduction in incidence during inflow and an increase during outflow. It is interesting to note that, for $\gamma = 5$ degrees, the rotor output torque is still positive in a very limited operating range during outflow, even though the cascade is misoriented with respect to the incoming flow. In this small range, the rotor efficiency is also positive, despite reaching a maximum value of just 17%. For the inflow phase, in the tested range of flow coefficients, i.e., the left side of the graphs in Figure 6, the zero-stagger Wells rotor reaches deep stall conditions, while it operates very close to the stall point when γ is set to 5 degrees, as shown in the torque coefficient plots in Figure 6a. Both the torque coefficient (before stall) and the pressure coefficient for any given value of ϕ decrease with the blade stagger angle, as the passage of the rotor becomes larger and the flow incidence smaller. On the contrary, the maximum efficiency grows with γ, while occurring for increasing values of ϕ (Figure 6c).

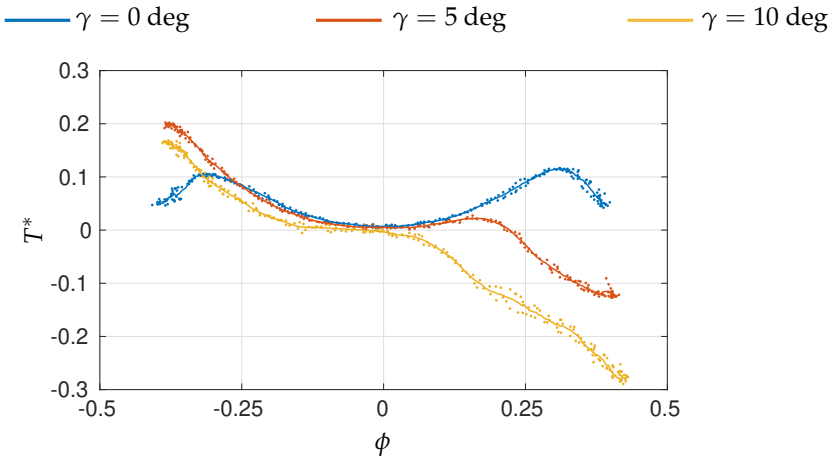

(**a**) Torque coefficient.

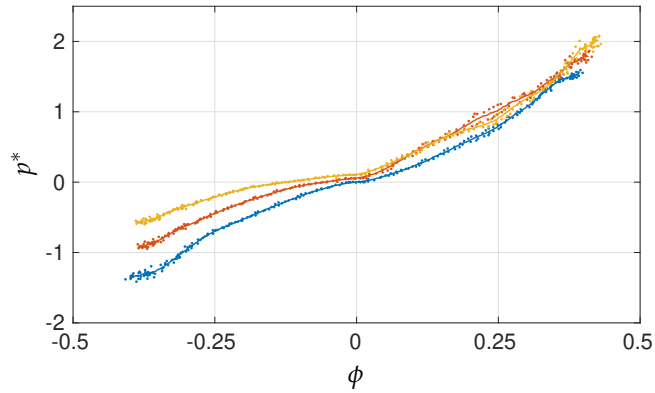

(**b**) Pressure coefficient.

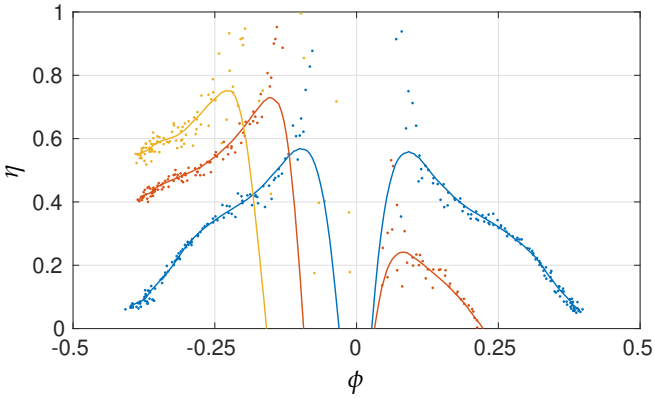

(**c**) Efficiency.

Figure 6. Performance coefficients for different blade stagger angles for a complete piston period (the dots correspond to measurement points).

3.2. Performance During the Inflow Phase

In this section, results are reported only for the inflow phase, for negative values of the flow coefficient ϕ, i.e., when restaggering produces a reduction in the incidence angle.

Figure 7 shows the performance curves for T^* and η in a more convenient and representative way.

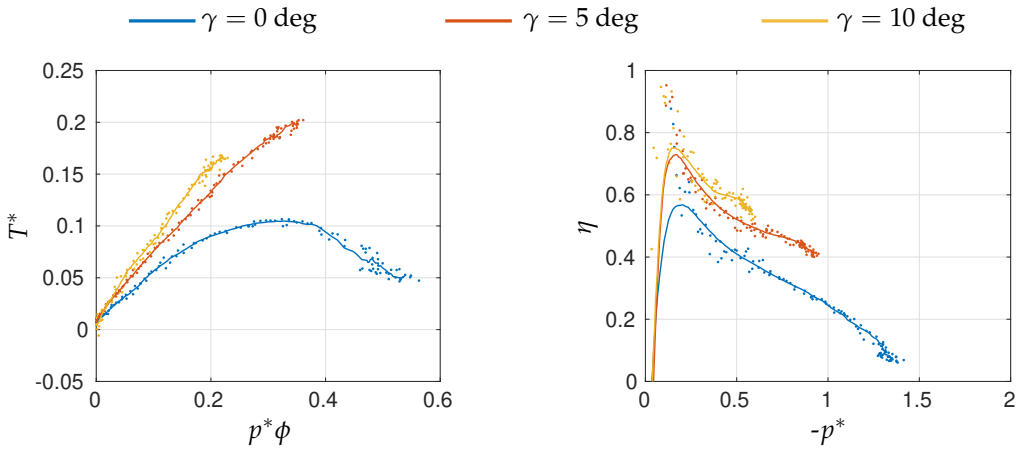

(**a**) Torque coefficient. (**b**) Efficiency.

Figure 7. Performance coefficients for different blade stagger angles during the inflow phase (the dots correspond to measurement points).

In Figure 7a, the torque coefficient, already reported in Figure 6a as a function of the flow coefficient, is now reported in terms of the non-dimensional available power provided by the OWC simulator, i.e., $p^*\phi \propto \Delta pQ$. Based on this parameter, the three geometries can be more appropriately compared in terms of their local aerodynamic behavior when working with the same available power, which can be assumed, at least as a first approximation, to remain unchanged when the three turbines are fitted to the same OWC. This representation clearly highlights that, for every value of $p^*\phi$, the output torque grows with the stagger angle, meaning that the staggered rotor is able to extract more energy than the non-staggered one, thus giving clear evidence of the performance improvement achievable with a variable-pitch rotor. This reflects on the rotor efficiency value, which is plotted in Figure 7b against the pressure coefficient, for the three values of γ. It is interesting to note that the best efficiency point, whose value grows with γ, occurs for almost the same value of p^*, regardless the value of γ. Although expected, this result should be taken into consideration for the definition of a control strategy based on varying the pitch angle to maximize the turbine efficiency.

The inlet flow has been reconstructed during the entire inflow phase (different values of ϕ) along the blade height, based on the measurements provided by the DIMCM probe. In Figure 8, the inlet flow is presented, for the three values of the stagger angle γ, in terms of the absolute tangential flow angle α and the radial flow angle ε.

The flow angle maps at the turbine inlet show an almost axial flow, with the absolute flow angle α_1 close to 90 degrees during the entire inflow phase, except near the inversions ($\phi \approx 0$). The potential effect due to the rotor's proximity is mostly reflected in a non-zero radial flow angle ε, which attains small positive values at all radial positions. This means that the inlet flow is moving from the hub to the tip, where the flow is allowed to cross the rotor more easily, thanks to lower solidity and to the tip clearance. It can be observed that this three-dimensional behavior is less pronounced as the blade stagger angle grows, due to the reduced obstruction obtained by rotating the blades, particularly in the hub region.

The outlet flow angles are reported in Figure 9, similarly to Figure 8 for the inlet flow angles.

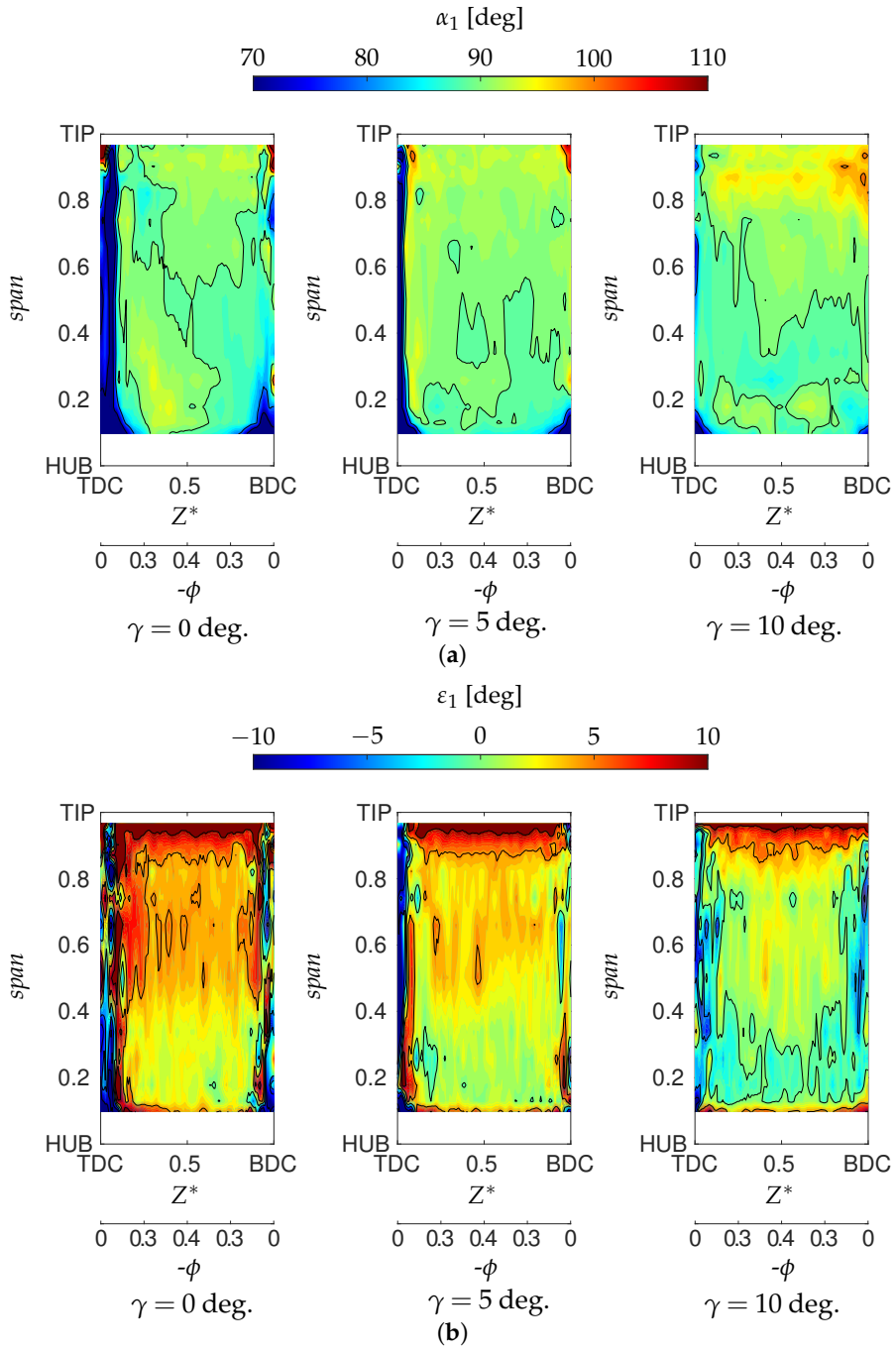

Figure 8. Inlet flow angles for the tested rotors. (**a**) Absolute flow angle; (**b**) Radial flow angle.

The absolute tangential flow angle α_2 presents its largest values in the lower half of the blade, while it decreases near the walls—particularly in the tip region, where it reaches values close to 90 degrees, as the flow becomes more axial due to the lower obstruction offered by the rotor and the presence of the tip clearance. The stall of the non-staggered rotor can be observed with the sharp drop in α_2 at the largest values of ϕ, particularly in the mid- to high-span region. The other rotors do not experience stall in the tested flow coefficient range, as already observed in Figure 7. Another important piece of information provided by the maps in Figure 9 is that the non-staggered Wells turbine is affected by tip stall, i.e., the flow separation originates in the tip region. In the stable operating range, i.e., in the absence of stall, the absolute flow angle for a fixed radial position is almost independent of ϕ, except near the inversions, for every value of the stagger angle γ. This result suggests that the value of α_2 is mostly governed by the rotor solidity, as predicted with potential

flow analysis on rotors with blades of negligible thickness [10,46] and already verified by previous experimental investigations [22,36]. The radial flow, described in Figure 9b, shows mostly negative flow angles along the blade span, which decrease as the stagger angle grows due to the lower obstruction offered by the rotor. Negative values of the radial flow angle mean that the flow is moving from higher to lower radii, as, after crossing the rotor, it tends to occupy the passage channel uniformly.

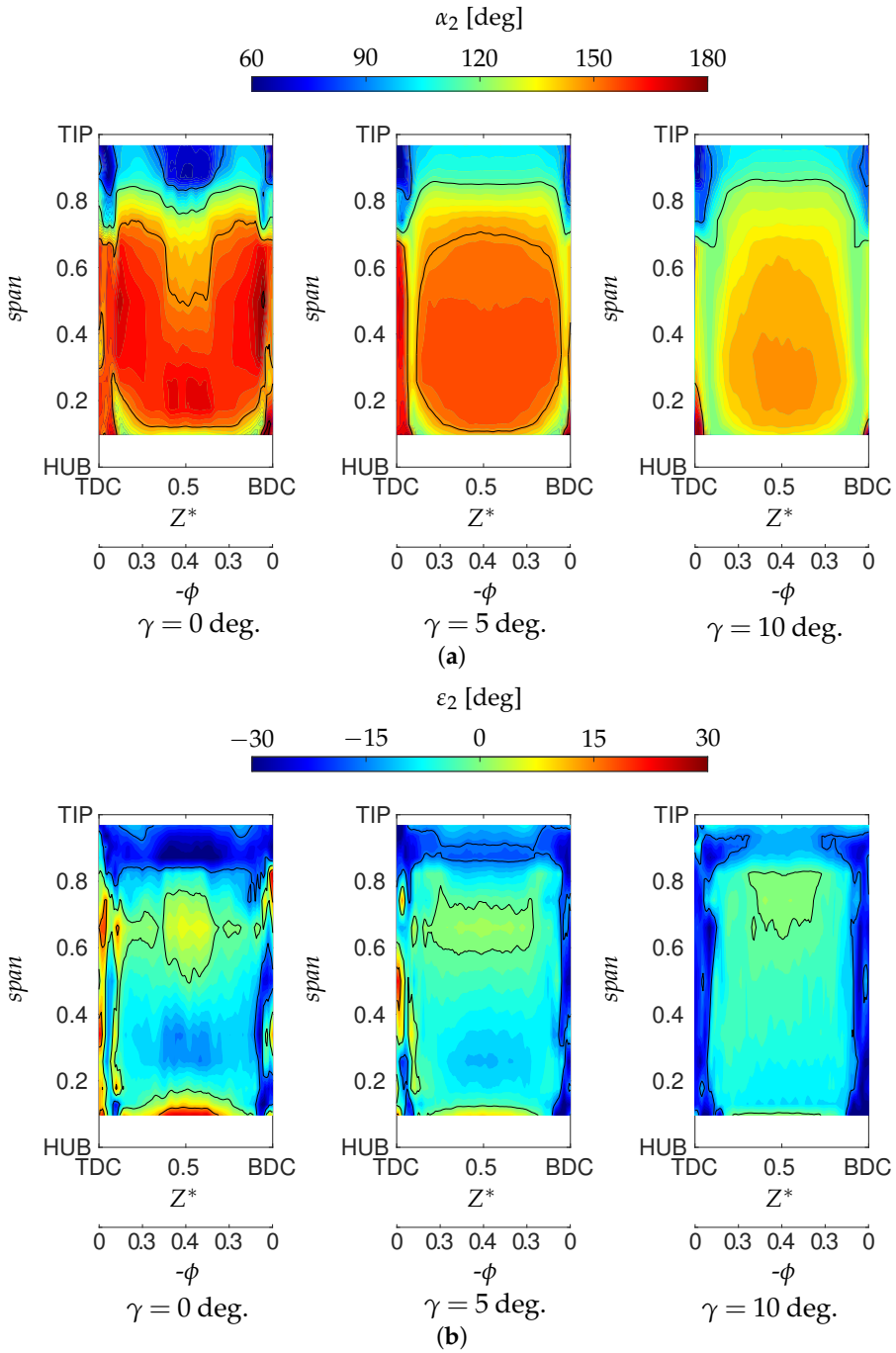

Figure 9. Outlet flow angles for the tested rotors. (**a**) Absolute flow angle; (**b**) Radial flow angle.

3.3. Local Performance for the Same Value of $p^*\phi$

In order to compare all rotors under the same operating conditions, the available power from the OWC has been chosen as the most representative parameter. A value of $p^*\phi = 0.2$ has been selected for this comparison, close to the maximum value available for all three turbines, as shown in Figure 7a. This value of $p^*\phi$ has been obtained with different

values of ϕ and p^* for the three rotors. These values are reported in Table 3 to aid the reader in the following comparisons.

Table 3. Operating conditions used for the local flow comparisons.

γ [deg]	$-\phi$	$-p^*$	$p^*\phi$
0	0.26	0.75	0.2
5	0.31	0.64	0.2
10	0.37	0.53	0.2

In Figure 10, the most relevant flow variables are shown for the different rotors, as a function of the blade span.

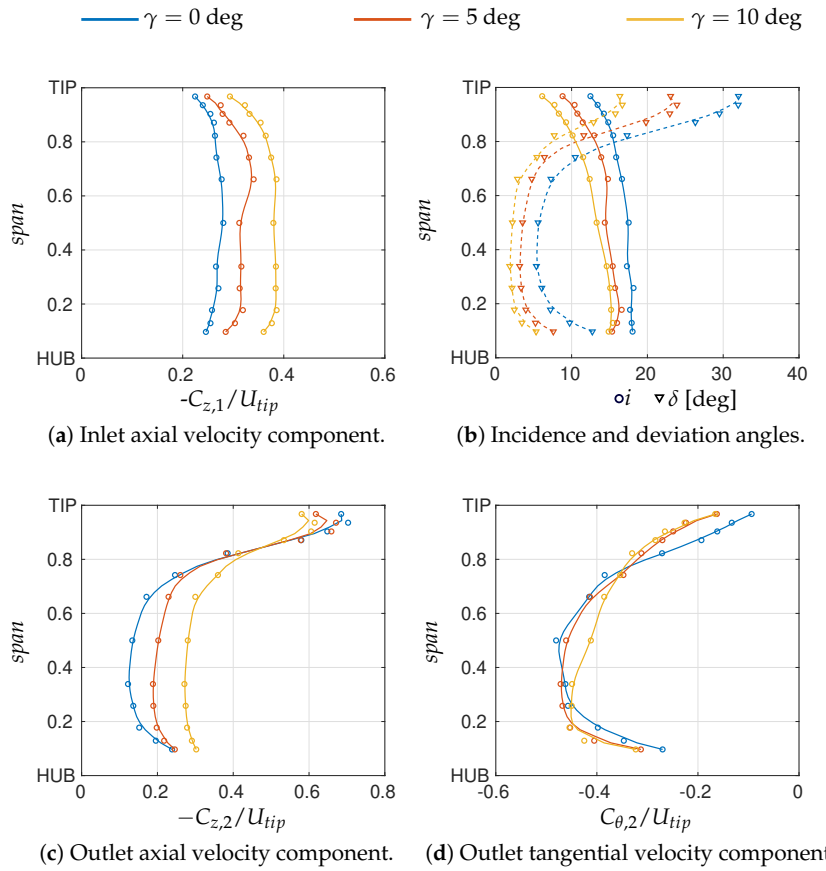

(**a**) Inlet axial velocity component. (**b**) Incidence and deviation angles.

(**c**) Outlet axial velocity component. (**d**) Outlet tangential velocity component.

Figure 10. Flow field characteristics at the inlet and the outlet of the rotor, for the three turbines with different stagger angles.

The trends of the inlet axial velocity component highlight that the rotors operate with different flow rates, growing with γ, under the same OWC pneumatic power, due to the lower obstruction. Nevertheless, the radial distribution of $C_{z,1}$ presents similar trends for all three configurations (blade stagger angles), with progressively lower values in the tip region, where the inlet flow is more three-dimensional, with larger values of the radial flow angle ε_1, as shown in Figure 8b. This effect, combined with the larger peripheral speed, results in a progressively smaller relative flow angle in the tip region, especially after 70% of the blade span. This is clearly shown in Figure 10b in terms of the incidence flow angle i, reported with solid lines and circle markers along the blade span. As expected, i is larger for the non-staggered rotor and it decreases with γ. The deviation angle, reported in Figure 10b with dotted lines and triangle markers, shows the opposite trend to γ, suggesting similar flow deflection angles for all tested turbines, except in the hub and tip regions. The larger

values of δ in the mid- to tip region clearly highlight the presence and influence of the leakage flow, being more evident in the outlet flow. The latter has been characterized in terms of the axial and tangential velocity components shown in Figure 10c,d, respectively. The different flow rates among the rotors are reflected in the smaller axial velocity in the lower 75% of the blade. In the tip region, $C_{z,2}$ attains larger values due to the presence of the leakage flow [36], which makes the flow highly three-dimensional, as observed in Figure 9b. It is interesting to note that, for larger stagger angles, this effect becomes progressively less intense due to the reduction in the pressure drop across the rotor, as reported in Table 3. As expected, the presence of the leakage flow results in a lower outlet tangential velocity contribution in the tip region. This reduction extends to the upper 40% of the blade span for the non-staggered rotor, suggesting a penalized work exchange in a wide portion of the blade height with respect to the staggered rotors. The comparison of the $C_{\theta,2}$ distributions for different values of γ suggests that the reduction in the exchanged specific work at midspan, obtained when increasing the stagger angle, is only partially compensated by higher values of the work near the walls, particularly in the hub region, with a more uniform distribution along the blade height.

The velocity vectors in Figure 11 provide a visualization of the relative flow field variation for different values of γ, in a quasi-blade-to-blade surface, i.e., neglecting the radial component.

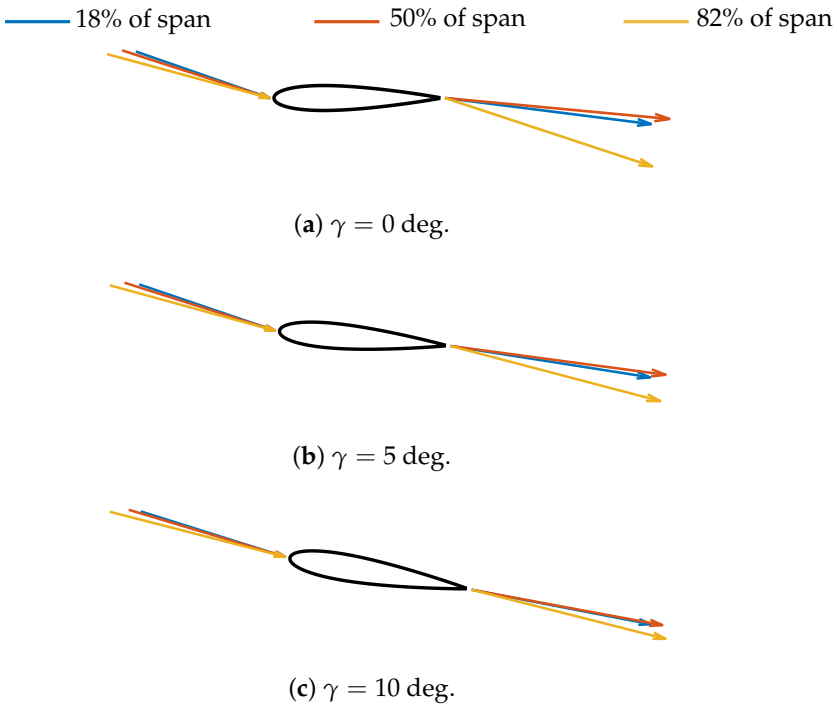

(**a**) $\gamma = 0$ deg.

(**b**) $\gamma = 5$ deg.

(**c**) $\gamma = 10$ deg.

Figure 11. Relative velocity vectors at the inlet and outlet of the three tested rotors, at different span positions.

These 2D representations clarify how the incidence flow angle decreases with γ, for the same value of available energy. It is evident that turbines with higher values of the stagger angle present lower three-dimensional effects, as shown by the smaller variation in the exit relative velocity in the radial direction.

In order to quantitatively compare the performance of the rotors, Figure 12 shows the radial distribution of the work coefficient ψ, of the aerodynamic efficiency η, and of the parameters representative of loss contributions, Y_P and ζ_{EX}.

As expected from the outlet tangential velocity comparison, the work coefficient ψ shows small differences from γ. In the midspan region, the non-staggered Wells rotor is able to produce slightly larger flow deflection and specific work, as the blade profile experiences a higher incidence in the absence of stall, as shown in Figure 10b. On the contrary, the tip and hub regions are more penalized for the non-staggered rotor due to the stronger three-dimensional flow—in particular, due to the leakage flow at larger radii. Only minor differences appear between the two staggered rotors, mostly in the midspan region, where ψ decreases with γ. As already discussed in Section 3.2, the different turbines can be more appropriately compared by means of the aerodynamic efficiency defined in Equation (1).

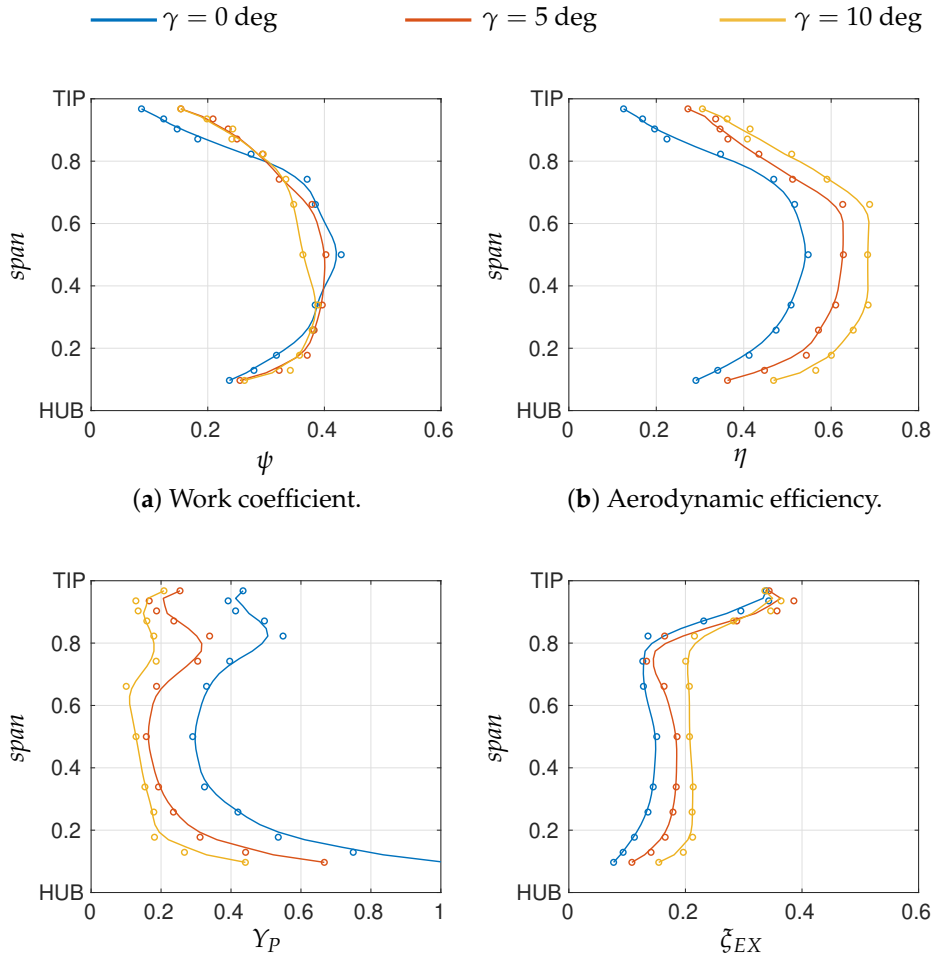

(**a**) Work coefficient. (**b**) Aerodynamic efficiency.

(**c**) Relative total pressure losses. (**d**) Exit kinetic energy losses.

Figure 12. Local performance variations along the blade span for the same available energy from the OWC, for the three rotor geometries.

The comparisons in Figure 12b give a clear indication of a poorly efficient turbine with non-staggered blades, while higher efficiency values are observed for the staggered turbines. The efficiency improvement, which has been observed along the entire blade radius, is due to the different operating conditions of the rotors. In fact, considering the efficiency definition in Equation (1), while the denominator, representing the available power, has been kept constant for these comparisons, the numerator increases with γ, as shown in Figure 7b. This is the consequence of what is observed in Figure 12a, where the work coefficient representing the specific work per unit of mass shows a relatively small reduction with γ in the presence of a larger flow rate (see Table 3).

A more detailed analysis of the rotor behavior has been conducted, evaluating the loss contributions Y_P and ξ_{EX}, representing the non-dimensional relative total pressure

loss and the residual kinetic energy at the rotor exit, respectively. It can be observed that, while ζ_{EX} grows with γ, as expected due to the larger values of the flow coefficient ϕ that the rotor operates at, the aerodynamic losses Y_P become progressively lower, with a maximum reduction at midspan of about 40%. This gives an important confirmation of the positive effect associated with the variation in the blade stagger angle, which determines an improvement in the rotor's aerodynamic behavior. As noticed for the non-staggered Wells rotor in [44], exit kinetic energy losses are less relevant than aerodynamic losses; hence, the efficiency is mostly driven by the latter contribution also when it is evaluated in the total-to-static formulation, with the exit kinetic energy considered completely lost.

4. Conclusions

A variable-pitch Wells rotor has been experimentally characterized in terms of both global and local performance. An aerodynamic four-hole pressure probe, designed and built at the DIMCM for this specific purpose, has been used to reconstruct the three-dimensional flow field along the blade height. Measurements have been conducted under non-stationary flow conditions, by reproducing regular (sinusoidal) wave motion with the available OWC simulator, for three different values of the blade stagger angle, seeking to produce a reduction in flow incidence during the inflow phase. The main results of this work can be summarized as follows.

- Both the output torque and pressure drop for any given stable operating condition decrease with the blade stagger angle; the maximum value of the efficiency grows and moves to larger flow rates, but it occurs almost for the same value of the pressure coefficient.
- When pitching the blades, the flow obstruction decreases, mitigating the three-dimensional characteristic of the inlet flow that naturally tends to move from the hub to the tip, due to the reducing solidity and to the tip clearance.
- For the same value of the available energy provided by the OWC, pitching the blades produces almost the same specific work along the blade height, while the local aerodynamic efficiency, at every radial position, grows with the stagger angle. This is due to the lower aerodynamic losses experienced in the presence of staggered blades.
- On the contrary, for the same value of the available energy provided by the OWC, the exit kinetic energy losses become larger with the blade stagger angle, although their relatively small contribution to the overall losses does not affect the trend in rotor efficiency.

This detailed investigation provides interesting results regarding the aerodynamics of the Wells blade row when its stagger angle is different from 90 degrees. Based on this information, different control strategies based on variable-pitch blades can be considered for the maximization of both the aerodynamic torque and the rotor efficiency.

Author Contributions: Conceptualization, P.P. and F.L.; methodology, P.P. and F.L.; software, F.L.; investigation, F.L.; data curation, F.L. and P.P.; writing—original draft preparation, F.L., P.P., T.G., F.C. and M.C.; writing—review and editing, F.L., P.P., T.G., F.C. and M.C.; visualization, F.L.; supervision, F.C.; project administration, F.C.; funding acquisition, F.C. All authors have read and agreed to the published version of the manuscript.

Funding: This research was funded by Italian Ministry of University and Research: e.INS—Ecosystem of Innovation for Next Generation Sardinia ECS00000038; Italian Ministry of University and Research: Network 4 Energy Sustainable Transition NEST; Italian Ministry of University and Research: APE-IRON—CUP F53D23009560001.

Data Availability Statement: The data presented in this study are available on request from the corresponding author.

Conflicts of Interest: The authors declare no conflicts of interest.

Nomenclature

C	absolute velocity
c	blade chord
η	efficiency
f	frequency of rotation
h	enthalpy per unit mass
i	incidence angle
P	total pressure
p	static pressure
p^*	static pressure drop coefficient
Q	volumetric flow rate
r	rotor radius
T	aerodynamic torque
t	tip clearance
T^*	torque coefficient
T_w	wave/piston period
U	peripheral speed
V	velocity
W	relative velocity
Y_P	relative total pressure loss coefficient
Z	piston position
z	number of blades

Greek symbols

α	$= 90 + \tan^{-1}(C_\theta / C_z)$ absolute flow angle
β	$= \tan^{-1}(C_z / W_\theta)$ relative flow angle
ϵ	$= \tan^{-1}(C_r / C_z)$ radial flow angle
γ	stagger angle
ν	hub-to-tip ratio
Ω	rotor angular velocity
ψ	work coefficient
ρ	fluid density
σ	rotor solidity
ξ_{EX}	exit kinetic energy losses

Subscripts and superscripts

1	inlet
2	outlet
hub	hub
r	radial
rel	relative flow
is	isentropic
t	total
θ	tangential
tip	tip
z	axial

Acronyms

CFD	computational fluid dynamics
OWC	oscillating water column
PTO	power take-off
WEC	wave energy converter

References

1. Gunn, K.; Stock-Williams, C. Quantifying the global wave power resource. *Renew. Energy* **2012**, *44*, 296–304. [CrossRef]
2. Guo, B.; Ringwood, J.V. A review of wave energy technology from a research and commercial perspective. *IET Renew. Power Gener.* **2021**, *15*, 3065–3090. [CrossRef]
3. López, I.; Andreu, J.; Ceballos, S.; Martínez de Alegría, I.; Kortabarria, I. Review of wave energy technologies and the necessary power-equipment. *Renew. Sustain. Energy Rev.* **2013**, *27*, 413–434. [CrossRef]
4. Aderinto, T.; Li, H. Review on Power Performance and Efficiency of Wave Energy Converters. *Energies* **2019**, *12*, 4329. [CrossRef]
5. Guo, C.; Sheng, W.; De Silva, D.G.; Aggidis, G. A Review of the Levelized Cost of Wave Energy Based on a Techno-Economic Model. *Energies* **2023**, *16*, 2144. [CrossRef]
6. Delmonte, N.; Barater, D.; Giuliani, F.; Cova, P.; Buticchi, G. Oscillating water column power conversion: A technology review. In Proceedings of the 2014 IEEE Energy Conversion Congress and Exposition (ECCE), Pittsburgh, PA, USA, 14–18 September 2014; pp. 1852–1859. [CrossRef]
7. Drew, B.; Plummer, A.R.; Sahinkaya, M.N. A review of wave energy converter technology. *Proc. Inst. Mech. Eng. Part A J. Power Energy* **2009**, *223*, 887–902. [CrossRef]
8. Curto, D.; Franzitta, V.; Guercio, A. Sea wave energy. A review of the current technologies and perspectives. *Energies* **2021**, *14*, 6604. [CrossRef]
9. Wells, Alan Arthur Fluid Driven Rotary Transducer. British Patent No. 1595700, 13 November 1976.
10. Raghunathan, S. The Wells air turbine for wave energy conversion. *Prog. Aerosp. Sci.* **1995**, *31*, 335–386. [CrossRef]
11. Shehata, A.; Xiao, Q.; Saqr, K.; Alexander, D. Wells turbine for wave energy conversion: A review. *Int. J. Energy Res.* **2017**, *41*, 6–38. [CrossRef]
12. Setoguchi, T.; Santhakumar, S.; Maeda, H.; Takao, M.; Kaneko, K. A review of impulse turbines for wave energy conversion. *Renew. Energy* **2001**, *23*, 261–292. [CrossRef]
13. Boake, C.; Whittaker, T.; Folley, M.; Ellen, H. Overview and initial operational experience of the LIMPET Wave Energy Plant. In Proceedings of the 12th International Offshore and Polar Engineering Conference, Kitakyushu, Japan, 26–31 May 2002; Volume 12.
14. Torre-Enciso, Y.; Ortubia, I.; de Aguileta, L.I.L.; Marqués, J. Mutriku Wave Power Plant: From the thinking out to the reality. In Proceedings of the 8th European Wave and Tidal Energy Conference, Uppsala, Sweden, 7–10 September 2009.
15. Gato, L.; Falcão, A.d.O. Aerodynamics of the Wells turbine. *Int. J. Mech. Sci.* **1988**, *30*, 383–395. [CrossRef]
16. Raghunathan, S.; Tan, C.P.; Ombaka, O.O. Performance of the Wells self-rectifying air turbine. *Aeronaut. J.* **1985**, *89*, 369–379. [CrossRef]
17. Amundarain, M.; Alberdi, M.; Garrido, A.J.; Garrido, I.; Maseda, J. Wave energy plants: Control strategies for avoiding the stalling behaviour in the Wells turbine. *Renew. Energy* **2010**, *35*, 2639–2648. [CrossRef]
18. Anderson, J. *Fundamentals of Aerodynamics*; McGraw-Hill Education: New York, NY, USA, 2010.
19. Barambones, O.; Cortajarena, J.; Gonzalez de Durana, J.; Alkorta, P. A real time sliding mode control for a wave energy converter based on a Wells turbine. *Ocean Eng.* **2018**, *163*, 275–287. [CrossRef]
20. Lekube, J.; Garrido, A.; Garrido, I. Variable speed control in Wells turbine-based oscillating water column devices: Optimum rotational speed. In Proceedings of the 6th International Conference on Power Science and Engineering ICPSE2017, St. Petersburg, Russia, 2–4 December 2017; Volume 136. [CrossRef]
21. Licheri, F.; Ghisu, T.; Cambuli, F.; Puddu, P. Wells turbine efficiency improvements: Experimental application of a speed control strategy. *J. Phys. Conf. Ser.* **2022**, *2385*, 012132. [CrossRef]
22. Licheri, F.; Puddu, P.; Cambuli, F.; Ghisu, T. Experimental investigation on a speed controlled Wells turbine for wave energy conversion. In *International Conference on Offshore Mechanics and Arctic Engineering*; Volume 8: Ocean Renewable Energy; American Society of Mechanical Engineers: New York, NY, USA, 2022; p. V008T09A077. [CrossRef]
23. M'zoughi, F.; Garrido, I.; Bouallègue, S.; Ayadi, M.; Garrido, A.J. Intelligent Airflow Controls for a Stalling-Free Operation of an Oscillating Water Column-Based Wave Power Generation Plant. *Electronics* **2019**, *8*, 70. [CrossRef]
24. Salter, S.H.; Taylor, J.R.M.; Caldwell, N.J. Power conversion mechanisms for wave energy. *Proc. Inst. Mech. Eng. Part M* **2002**, *216*, 1–27. [CrossRef]
25. Gato, L.M.C.; de O. Falcão, A.F. Aerodynamics of the Wells turbine: Control by swinging rotor-blades. *Int. J. Mech. Sci.* **1989**, *31*, 425–434. [CrossRef]
26. Gato, L.M.C.; Eça, L.R.C.; Falcão, A.F.d.O. Performance of the Wells Turbine With Variable Pitch Rotor Blades. *J. Energy Resour. Technol.* **1991**, *113*, 141–146. [CrossRef]
27. Gato, L.M.C.; Webster, M. An experimental investigation into the effect of rotor blade sweep on the performance of the variable-pitch Wells turbine. *Proc. Inst. Mech. Eng. Part A J. Power Energy* **2001**, *215*, 611–622. [CrossRef]
28. Kim, T.; Setoguchi, T.; Takao, M.; Kaneko, K.; Santhakumar, S. Study of turbine with self-pitch-controlled blades for wave energy conversion. *Int. J. Therm. Sci.* **2002**, *41*, 101–107. [CrossRef]
29. Tease, W.K. *Dynamic Response of a Variable Pitch Wells Turbine*; Report; Turbine Department, Wavegen: Inverness, UK, 2007.

30. Licheri, F.; Climan, A.; Puddu, P.; Cambuli, F.; Ghisu, T. Numerical study of a Wells turbine with variable pitch rotor blades. *Energy Procedia* **2018**, *148*, 511–518. [CrossRef]
31. Licheri, F.; Ghisu, T.; Cambuli, F.; Puddu, P. Experimental characterization of a variable-pitch Wells turbine. *J. Phys. Conf. Ser.* **2024**, *2893*, 012131. [CrossRef]
32. Sarmento, A.J.N.A.; Gato, L.M.C.; Falcão, A.F.d.O. Turbine-controlled wave energy absorption by oscillating water column devices. *Ocean Eng.* **1990**, *17*, 481–497. [CrossRef]
33. Taylor, J.R.; Caldwell, N. Design and Construction of the Variable-Pitch Air Turbine for the Azores Wave Energy Plant. In Proceedings of the 3rd European Wave Power Conference, Patras, Greece, 30 September–2 October 1998; pp. 328–337.
34. Falcão, A.F.O.; Sarmento, A.J.N.A.; Gato, L.M.C.; Brito-Melo, A. The Pico OWC wave power plant: Its lifetime from conception to closure 1986–2018. *Appl. Ocean Res.* **2020**, *98*, 102104. [CrossRef]
35. Paderi, M.; Puddu, P. Experimental investigation in a Wells turbine under bi-directional flow. *Renew. Energy* **2013**, *57*, 570–576. [CrossRef]
36. Licheri, F.; Ghisu, T.; Cambuli, F.; Puddu, P. Experimental reconstruction of the local flow field in a Wells turbine using a three-dimensional pressure probe. *Energy* **2024**, *296*, 131062. [CrossRef]
37. Licheri, F.; Ghisu, T.; Cambuli, F.; Puddu, P.; Carta, M. Effects of tip gap size and aspect ratio on the performance of a Wells turbine. *Renew. Energy* **2025**, *242*, 122389. [CrossRef]
38. Licheri, F.; Ghisu, T.; Cambuli, F.; Puddu, P.; Carta, M. Experimental results in a variable-pitch Wells rotor. In Proceedings of the 16th European Turbomachinery Conference, Hannover, Germany, 24–28 March 2025; Paper n. ETC2025-254. Available online: https://www.euroturbo.eu/publications/conference-proceedings-repository/ (accessed on 8 April 2023).
39. Peng, J.; Hu, C.; Yang, C. Influence of incoming wave conditions on the hysteretic behavior of an oscillating water column system for wave energy conversion. *Ocean Eng.* **2023**, *280*, 114828. Corrigendum in *Ocean Eng.* **2023**, *290*, 116209. [CrossRef]
40. Bryer, D.W.; Pankhurst, R.C. Pressure-Probe Methods for Determining Wind Speed and Direction. *Aeronaut. J.* **1971**, *75*, 126. [CrossRef]
41. Shannon, C. Communication in the Presence of Noise. *Proc. IRE* **1949**, *37*, 10–21. [CrossRef]
42. Horlock, J. Losses and efficiencies in axial-flow turbines. *Int. J. Mech. Sci.* **1960**, *2*, 48–75. [CrossRef]
43. Dixon, S.L.; Hall, C.A. *Fluid Mechanics and Thermodynamics of Turbomachinery*, 6th ed.; Elsevier, Inc.: Amsterdam, The Netherlands, 2010.
44. Licheri, F.; Ghisu, T.; Cambuli, F.; Puddu, P. Detailed investigation of the local flow-field in a Wells turbine coupled to an OWC simulator. *Renew. Energy* **2022**, *197*, 583–593. [CrossRef]
45. Coleman, H.W.; Glenn Steel, W., Jr. *Experimentation, Validation, and Uncertainty Analysis for Engineers*, 3rd ed.; John Wiley & Sons, Ltd.: New York, NY, USA, 2009. [CrossRef]
46. Falcão, A.F.O.; Gato, L.M.C. 8.05—Air Turbines. In *Comprehensive Renewable Energy*; Elsevier: Oxford, UK, 2012; pp. 111–149. [CrossRef]